EFFECTS OF STREAM SURFACE INCLINATION ON TIP LEAKAGE FLOW FIELDS IN COMPRESSOR ROTORS

Masato Furukawa, Kazuhisa Saiki, Kenya Nagayoshi, Motoo Kuroumaru and Masahiro Inoue
Department of Energy and Mechanical Engineering
Kyushu University
Fukuoka 812-81
Japan

ABSTRACT

Experimental and computatinnal results nf tip leakage flnw fields in a diagnnal flnw rotor at the design flow rate are compared with those in an axial flow rotor. In the diagonal flow rotor, the casing and hub walls are inclined at 25 degrees and 45 degrees, respectively, to the axis of rotation, and the blade has airfoil sections with almost the same tip solidity as that of the axial flow rotor. It is found out that "breakdown" of the tip leakage vortex occurs at the aft part of the passage in the diagonal flow rotor. The "vortex breakdown" causes significant changes in the nature of the tip leakage vortex: disappearance of the vortex core, large expansion of the vortex, and appearance of low relative velocity region in the vortex. These changes result in the behavior of the tip leakage flnw substantially different from that in the axial flow rotor: no rolling-up of the leakage vortex downstream of the rotnr, disappearance of the casing pressure trough at the aft part of the rotor passage, large spread of the low-energy fluid due to the leakage flow, much larger growth of the casing wall boundary layer, and considerable increase in the absolute tangential velocity in the casing wall boundary layer. The vortex breakdown influences the overall performance, also: large reduction of efficiency with the tip clearance, and low level of noise.

INTRODUCTION

Tip leakage flow fields in axial flow compressors have been studied by many researchers since Rains' work (1954), because of their impact on compressor stability and performance (Smith Jr., 1970). Especially, they have been highlighted for the last decade, and its complex flow mechanism is getting more and more clarified by numerous experimental and numerical works (Inoue et al., 1986; Hah, 1986; Murthy and Lakshminarayana, 1986; Dawes, 1987; Inoue and Kuroumaru, 1989; Chen, et al., 1991; Storer and Cumpsty, 1991; Moyle et al., 1992; Adamczyk et al., 1993; Stauter, 1993; Lakshminarayana et al., 1995; Zierke et al., 1995; Foley and Ivey, 1996; Suder and Celestina, 1996; Kang and Hirsch, 1996). The distinctive feature of the flow structure is the rolling-up of the tip leakage vnrtex and its interaction with secondary flows.

On the other hand, one of the authors has once studied on possibility of a diagonal flow compressor rotnr as a first stage of a multi-stage compressor, because its loading coefficient can be about one and a half times as high as that of an axial flow rotor. On the basis of the quasi-three-dimensional design method proposed by Inoue et al. (1980), a diagonal flow rotor with NACA 65 series profile was designed and tested (Inoue et al., 1984). The blade solidity at the tip was almost the same as that of the axial compressor rotor which the authors used to investigate the structure of the tip leakage flow (Inoue et al., 1986). The high loading coefficient required was obtained notwithstanding small number of blades, and the noise level was considerably low, compared with the axial flow rotor. However, an effect of the tip clearance on tbe rotor performance was much larger in comparison with the axial rotor case: the reduction of efficiency with the tip clearance was about three times as large as that of the axial flow rotor. Recently, the authors reassembled the diagonal flow rotor in the low-speed rotating cascade equipment of Kyushu University, and surveyed the internal flow field to examine a cause of the large reduction of efficiency with the tip clearance (Furukawa et al., 1995a). The phase-locked flow fields measured just behind the rotor indicated that there was no vortex rolling-up even in the case of a large tip clearance.

Goto (1992a, b) studied internal flows in a mixed-flow pump impeller with various tip clearances by experiments and numerical simulations. His results showed that there was substantial difference in the secondary flow field between axial-flow and mixed-flow impellers.

In this study the tip leakage flow fields at the design flow rate are compared between the axial and the diagonal flow rotor which have similar blade solidities at the tip section, to clarify the reason why the reducing rate of efficiency with the tip clearance is much larger and the noise level is much less for the diagonal flow rotor. The experimental data used in the comparison are tangentially averaged velocity distributions, phase-locked averaged velocity distributions just downstream of

Presented at the International Gas Turbine & Aeroengine Congress & Exhibition
Orlando, Florida — June 2–5, 1997
This paper has been accepted for publication in the Transactions of the ASME
Discussion of it will be accepted at ASME Headquarters until September 20, 1997

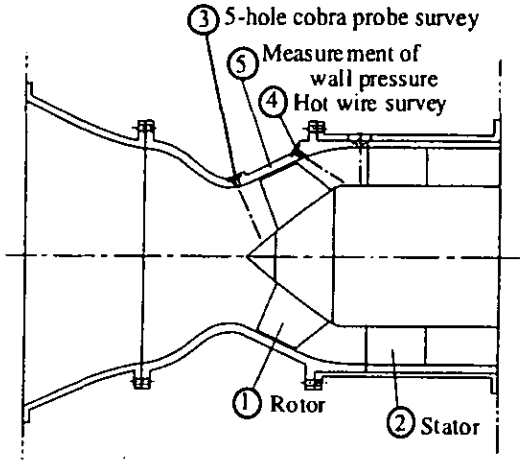

Fig.1 Meridional view of diagonal flow rotor

the rotors, and phase-locked averaged pressure distributions on the casing walls. Three-dimensional viscous flow simulations are carried out by a high-resolution upwind scheme based on a TVD formulation with a cell-centered finite volume method, to investigate the detailed behavior of the tip leakage flows.

EXPERIMENTAL APPARATUS AND PROCEDURE

Diagonal Flow Rotor

The experimental investigation was performed using the diagonal flow rotor with high specific speed shown in Fig. 1. Design specifications of the rotor are summarized in Table 1 where the flow coefficient, ϕ, and the total pressure rise coefficient, ψ, are defined as

$$\phi = \frac{Q}{U_t \pi \left(D_t^2 - D_h^2 \right) / 4} \tag{1}$$

$$\psi = \frac{\Delta P}{\rho U_t^2 / 2} \tag{2}$$

where Q is the volume flow rate, ΔP is the total pressure rise, U_t is the blade tip speed at the rotor exit, ρ is the density, D_t and D_h denote the tip and hub diameters at the rotor exit, respectively. In the rotor the shapes of the hub and casing walls were cones with inclinations of 45 degrees and 25 degrees, respectively, to the axis of rotation. The design vortex type of the rotor was a free vortex with an axial inlet condition. The equivalent diffusion ratio in Table 1 is based on an extension of that of Lieblein to include changes in radius and axial velocity through the blade row derived by Klapproth (1959).

Blades of the rotor were made up of NACA 65 series airfoil sections designed by the quasi-three-dimensional method of Inoue et al. (1984). In the design method, a meridional through-flow was first solved by a streamline curvature method to determine averaged stream surfaces, and then the stream surfaces were transformed conformally into two-dimensional planes on which blade elements were selected by means of a two-dimensional cascade data. Cascade geometries of the blade elements were corrected theoretically by taking account of effects

Table 1 Design specifications of diagonal flow rotor

Flow coefficient	$\phi = 0.563$
Total pressure rise coefficient	$\psi = 0.75$
Vortex design	Free vortex
Tip diameter	$D_t = 400$ mm (rotor exit)
Hub-tip ratio	$\nu = 0.75$ (rotor exit)
Blade profile	NACA 65 series
Number of blades	6
Blade thickness	10%(root), 4%(tip)
Solidity at tip	1.054
Chord length at tip	157 mm
Equivalent diffusion ratio at tip	$D_{eq} = 1.64$
Hub inclination	45°
Casing inclination	25°

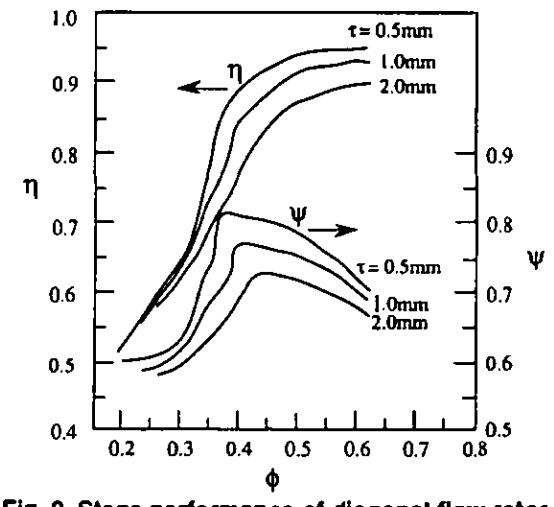

Fig. 2 Stage performance of diagonal flow rotor

due to the stream surface inclination and the stream surface thickness variation. Lastly the blade elements on the two-dimensional planes were retransformed into the physical space.

The blade tip clearance was varied by moving the rotor in the axial direction. Experiments were performed for three blade tip clearances of τ = 0.5, 1.0 and 2.0 mm, which corresponded to 0.3, 0.6 and 1.3 percent of tip chord, respectively. Figure 2 shows the stage performance of the diagonal flow rotor. In the case of the minimum clearance, the performance satisfied the design point, and the efficiency was 95 percent at the design flow rate.

Flow fields upstream and downstream of the rotor and pressure distributions on the casing wall were measured, as shown in Fig. 1, at the design flow rate (ϕ = 0.563) for the three different tip clearances. The flow measurements were made at a rotor rotational speed of 1300 rpm. Upstream of the rotor the survey of a 5-hole cobra probe was carried out. In all the experiments the meridional displacement thickness of the casing wall boundary layer was 0.3 percent of tip chord upstream of the rotor. On the other hand, downstream of the rotor phase-locked flow fields were obtained by a constant temperature hot-wire anemometer and a periodic multisampling and averaging technique with a computerized data acquisition system (Kuroumaru et al. 1982).

Table 2 Design specification of axial flow rotor

Flow coefficient	$\phi = 0.5$
Total pressure rise coefficient	$\Psi = 0.4$
Vortex design	Free vortex
Tip diameter	D_t =449 mm
Hub-tip ratio	$\nu = 0.6$
Blade profile	NACA 65 series
Number of blades	12
Blade thickness	10%(root), 6%(tip)
Solidity at tip	1.00
Chord length at tip	117.5 mm
Equivalent diffusion ratio at tip	D_{eq} = 1.43

The hot-wire sensor was a slanted single tungsten wire with a diameter of 5 μm, an effective length of 1 mm and a slant angle of 45 degrees. The hot-wire measurements were made at 23 spanwise positions. In each spanwise position, the hot-wire signals were sampled at 300 tangential points relative to the rotor. The 300 tangential points covered three successive blade passages. Phase-locked pressure distributions on the casing wall were obtained by also applying the periodic multisampling and averaging technique to pressure measurements using a high response pressure sensor. The pressure sensor was installed on the casing wall in a similar manner to that used in the previous study (Inoue and Kuroumaru, 1989). The casing wall pressure measurements were performed at 13 axial positions, and pressure samplings in each axial position were made at 200 tangential points corresponding to two successive blade passages.

Axial Flow Rotor

Experimental results for the diagonal flow rotor were compared with those for the axial flow rotor presented in the previous papers (Inoue et al., 1986; Inoue and Kuroumaru, 1989). The axial flow rotor had design specifications given in Table 2. The hub and casing walls were cylindrical, that is, had no inclination to the axis of rotation.

Experiments were performed for five different tip clearances of τ = 0.5, 1.0, 2.0, 3.0 and 5.0 mm (0.4, 0.8, 1.7, 2.6 and 4.3 percent of tip chord, respectively). Phase-locked velocity fields downstream of the rotor (Inoue et al., 1986) and phase-locked pressure fields on the casing wall (Inoue and Kuroumaru, 1989) were measured at the design flow condition with a rotor rotational speed of 1300 rpm in the same way as the diagonal flow rotor. The displacement thickness of the casing wall boundary layer at the inlet was 0.6 percent of tip chord in all the experiments.

NUMERICAL ANALYSIS

Numerical Scheme

We performed numerical flow simulations in order to investigate the tip leakage flow field inside the rotor passage which was not able to be measured by our experimental apparatus. In the numerical simulations the compressible Navier-Stokes equations were solved by an unfactored implicit upwind relaxation scheme (Furukawa et al., 1995b). The numerical method used is outlined in the following.

The three-dimensional, Reynolds-averaged Navier-Stokes

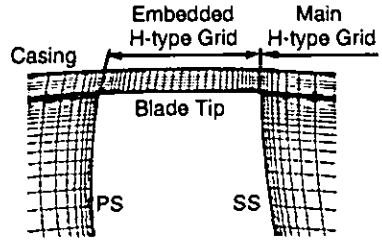

Fig. 3 Typical cross-sectional view of computational grid near blade tip

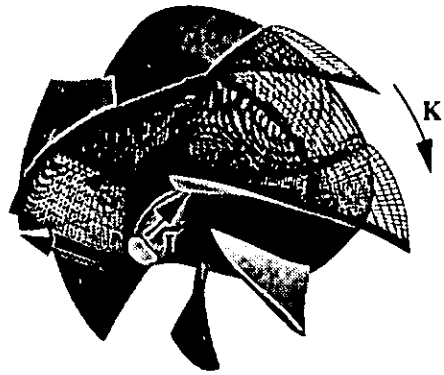

(a) Perspectiva view

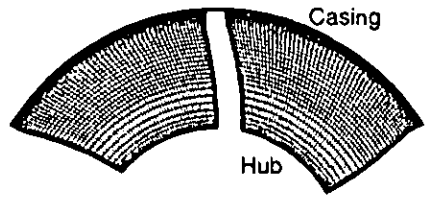

(b) Cross-sectional view

Fig. 4 Computational grid for diagonal flow rotor

equations were discretized in space using a cell-centered finite volume formulation and in time using the Euler implicit method. To sharply capture the tip leakage vortex near the casing wall, the inviscid fluxes were evaluated by a high-resolution upwind scheme based on a TVD formulation (Furukawa et al., 1991; Inoue and Furukawa, 1994) where a Roe's approximate Riemann solver of Chakravarthy (1986) and a third-order accurate MUSCL approach of Anderson et al. (1986) with the Van Albada limiter were implemented. Most of numerical flow solvers for turbomachinery problems, however, are based on artificial dissipative schemes in which the inviscid terms are discretized in central differencing manners with artificial dissipation terms. According to studies on the application of high-resolution upwind schemes to the Navier-Stokes equations by van Leer et al. (1987), and Swanson and Turkel (1993), it is found that built-in numerical dissipation terms introduced by the high-resolution upwind schemes using Riemann solvers such as Roe's (Roe, 1981) and Osher's (Osher and Chakravarthy, 1983) automatically become much smaller in boundary layers than those introduced by the artificial dissipative schemes so as not to mask the physical diffusion in the boundary layers. It should be noted that

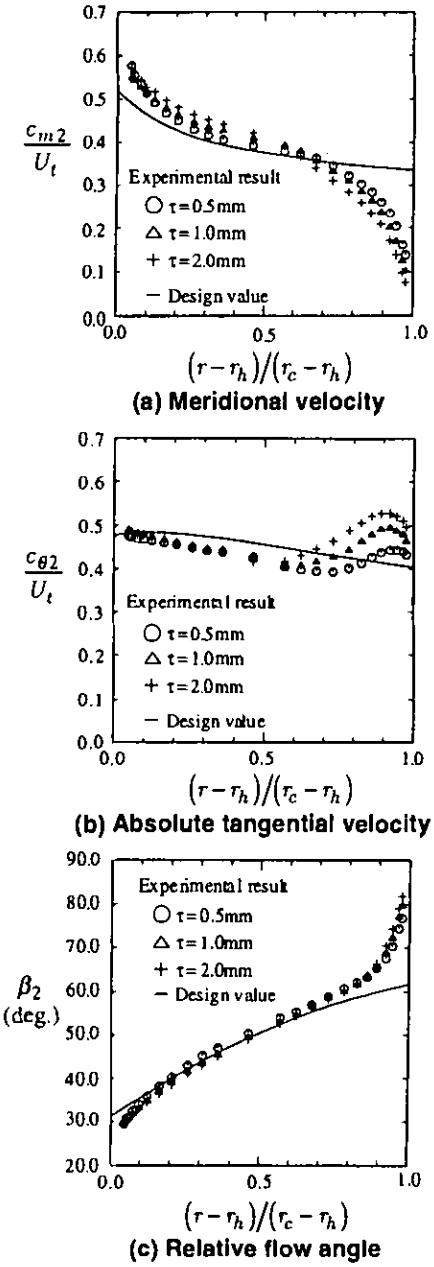

Fig. 5 Tangentially averaged flow distributions downstream of diagonal flow rotor

the high-resolution upwind schemes based on the Riemann solvers have excellent shear-layer capturing capability as well as shock-wave capturing one. In the present scheme, the viscous fluxes were determined in a central differencing manner with Gauss's theorem, and the algebraic turbulence model of Baldwin and Lomax (1978) was employed to estimate the eddy viscosity. The boundary layer transition was determined in accordance with an original criterion of transition in the Baldwin and Lomax model. Unfactored implicit equations derived with no approximate factorization were solved by a point Gauss-Seidel relaxation method. The present scheme was stable up to a Courant number of about 100.

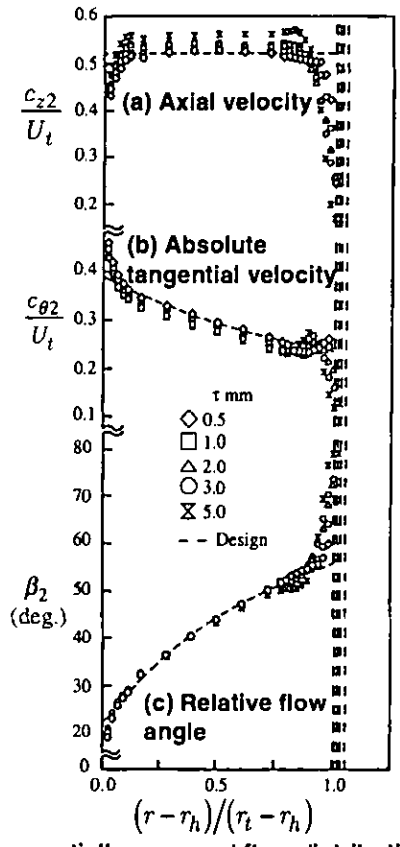

Fig. 6 Tangentially averaged flow distributions downstream of axial flow rotor, from Inoue et al. (1986)

The present scheme has been already applied to calculations of a trailing edge vortex shedding in a transonic turbine cascade (Furukawa et al., 1992) and a three-dimensional flow in a diagonal flow rotor with a vortex type of a constant tangential velocity (Furukawa et al., 1995b). In these previous studies the validity of the scheme has been presented by comparing numerical results with experimental ones.

Computational Grids

A composite grid system with structured H-type grids was used to simulate the tip leakage flow accurately. A computational domain was divided into two zones. One zone was a main flow region outside the blade tip clearance, and the other was the tip clearance region. In each zone a structured H-type grid was generated as shown in Fig. 3. The main grids for both the diagonal and axial flow rotors consisted of 80 cells in the streamwise (I) direction (52 cells on the blade), 64 cells in the spanwise (J) direction, and 64 cells in the pitchwise (K) direction, as shown in Fig. 4. In order to sharply capture the tip leakage vortex, grid resolution was kept high even at the midpitch near the casing, as seen in Fig. 4(b). The grid embedded in the blade tip clearance consisted of $52\times32\times16$ cells in the chordwise, pitchwise and spanwise directions, respectively, for both rotors. The whole grid system had 354,304 cells. The ratio of the minimum grid spacing on solid walls to the blade tip chord length was under 5×10^{-5} to evaluate the viscous fluxes at the walls by applying the no-slip and adiabatic conditions

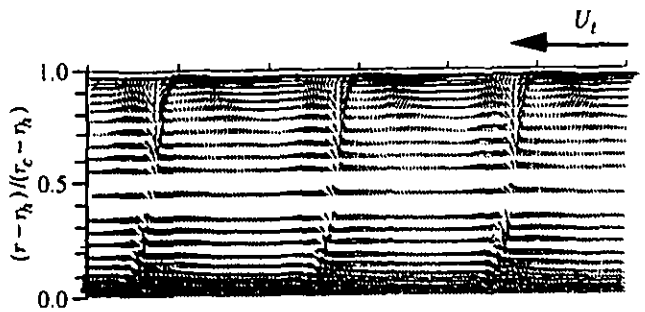

(a) Blade tip clearance of τ = 0.5 mm

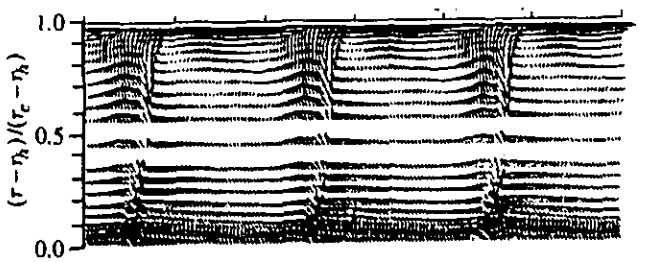

(b) Blade tip clearance of τ = 1.0 mm

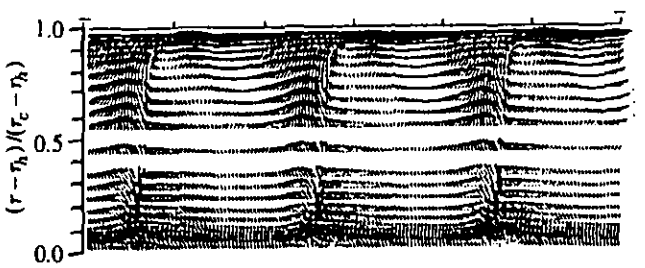

(c) Blade tip clearance of τ = 2.0 mm

Fig. 7 Secondary flow vectors downstream of diagonal flow rotor

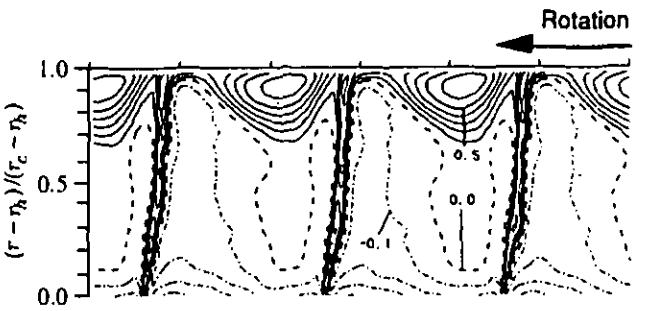

(a) Blade tip clearance of τ = 0.5 mm

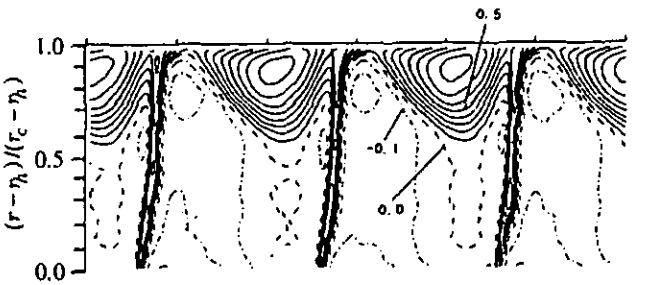

(b) Blade tip clearance of τ = 1.0 mm

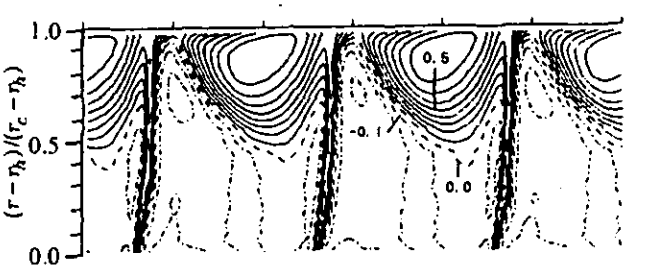

(c) Blade tip clearance of τ = 2.0 mm

Fig. 8 Relative kinetic energy defect distributions downstream of diagonal flow rotor

with no wall function method.

Boundary and Computational Conditions

Boundaries of the computational domain are formed by cell interfaces for the cell-centered finite volume approach. Hence, the boundary conditions must be imposed by the fluxes through the boundaries. In the present scheme, fictitious cells were introduced just outside all the boundaries, and values of conserved variables satisfying boundary conditions were given at the fictitious cells. Using the fictitious cells, numerical fluxes through the boundaries were evaluated in the same way as interior cell interfaces. This treatment of the boundary conditions prevented nonphysical reflections at the inflow and outflow boundaries, because the inviscid fluxes through the boundaries were evaluated according to the approximate Riemann solver in which the signal propagation properties of the Euler equations were simulated. It should be noted that the outflow boundary conditions implemented in the present scheme allowed the pressure to vary on the boundary according to effects of streamline curvature and swirl. Details of the boundary conditions are described in the previous paper (Furukawa et al., 1995b).

In order to simulate the flow fields on the same flow conditions as the experiments, the inlet boundary conditions were given by experimental results measured upstream of the rotors using a 5-hole cobra probe. The numerical simulations were carried out at the design flow rate for both the diagonal and axial flow rotors with the blade tip clearance of τ = 2.0 mm.

RESULTS AND DISCUSSION

Tangentially Averaged Flows Downstream of Rotor

Spanwise distributions of the tangentially averaged flow properties downstream of the diagonal flow rotor are shown in Fig. 5. The tangentially averaged flow distributions are obtained by averaging the phase-locked flow data measured with the hot-wire anemometer. In

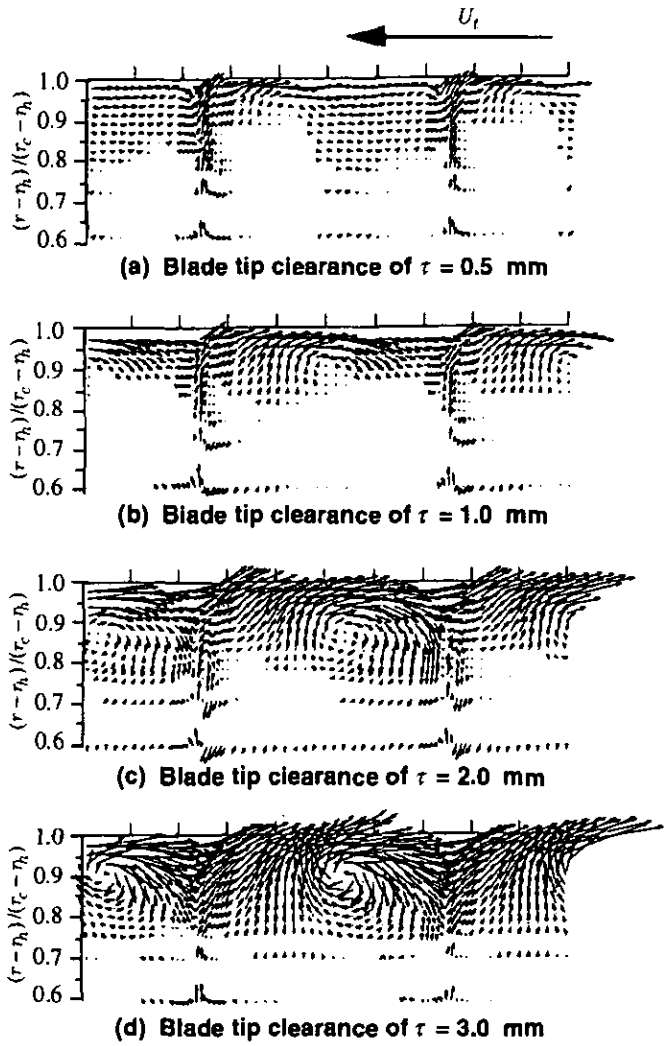

Fig. 9 Secondary flow vectors downstream of axial flow rotor, from Inoue et al. (1986)

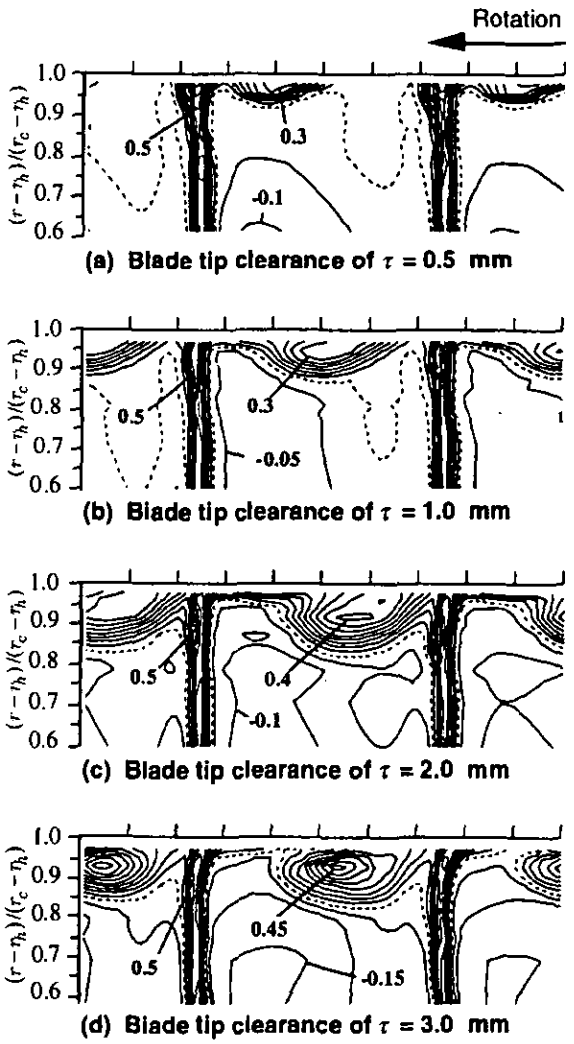

Fig. 10 Relative kinetic energy defect distributions downstream of axial flow rotor, from Inoue et al. (1986)

the figure the abscissa represents a nondimensional distance from the hub wall, and symbols and solid lines denote the experimental results and the design values, respectively. The velocity is normalized by the blade tip speed at the rotor exit, U_t. According to the meridional velocity distributions, the growth of the boundary layer is suppressed on the hub wall. On the other hand, the boundary layer on the casing wall is so thick that its thickness reaches about 50 percent of span height in the case of τ = 2.0 mm. As compared with tangentially averaged flow distributions downstream of the axial flow rotor, which are shown in Fig. 6, it is readily seen that the casing wall boundary layer in the diagonal flow rotor is much thicker than that in the axial flow rotor with the larger tip clearances. This implies that the tip leakage flow in the diagonal flow rotor causes the much larger growth of the casing wall boundary layer. And furthermore, in contrast to the axial flow rotor, the absolute tangential velocity downstream of the diagonal flow rotor increases considerably in the casing wall boundary layer as seen in Fig. 5(b).

Phase-Locked Flow Fields Downstream of Rotor

The phase-locked velocity fields measured just downstream of the diagonal flow rotor are compared with those for the axial flow rotor. Figures 7 and 8 show secondary flow vectors and relative kinetic energy defect distributions for the diagonal flow rotor. The secondary flow vector is defined by a velocity component perpendicular to the design relative flow direction, and the relative kinetic energy defect, ζ_d, is defined as

$$\zeta_d = \left(w^{*2} - w^2\right) \Big/ w^{*2} \tag{3}$$

where w and w^* denote the measured and design values of the relative flow velocity, respectively. The phase-locked velocity fields downstream of the axial flow rotor are also presented in Figs. 9 and 10 where only the flow field from 60 percent span to the casing is shown. It should be noted that the contours of ζ_d shown by the broken line correspond to ζ_d of 0, and that the increments of ζ_d in the contours shown in Figs. 8 and 10 are 0.1 and 0.05, respectively.

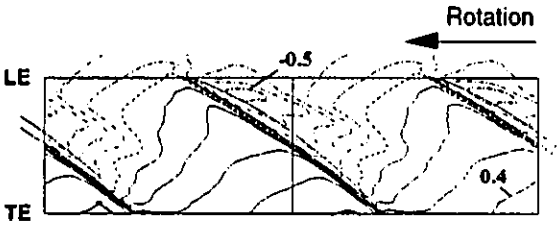

(a) Diagonal flow rotor with tip clearance of τ = 2.0 mm

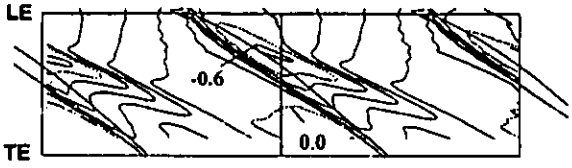

(b) Axial flow rotor with tip clearance of τ = 2.0 mm, from Inoue and Kuroumaru (1989)

Fig. 11 Casing wall pressure distributions

In the secondary flow fields downstream of the axial flow rotor, the small rolling-up of the leakage vortex is visible even in the case of τ = 1.0 mm (0.8 percent of tip chord) shown in Fig. 9(b), and the distinct rolling-up is observed in the case of τ > 1.0 mm.

In contrast to the axial flow rotor, no rolling-up of the tip leakage vortex is observed in the secondary flow fields downstream of the diagonal flow rotor shown in Fig. 7. And besides, Fig. 8 indicates that spread of the low-energy fluid accumulating on the casing is extremely large, compared with that for the axial flow rotor (Fig. 10). The spread in the spanwise direction even for the smallest tip clearance is more extensive than that for the axial flow rotor with the largest clearance. The spread reaches about a half of span in the case of τ = 2.0 mm. This corresponds well to the large growth of the casing wall boundary layer shown in Fig. 5(a). The above implies that the behavior of the tip leakage flow in the diagonal flow rotor is substantially different from that in the axial flow rotor.

Phase-Locked Pressure Fields on Casing Wall

The phase-locked distributions of the ensemble-averaged pressure on the casing wall in the diagonal and axial flow rotors are shown in Fig. 11, respectively. The distributions are presented by the static pressure coefficient, C_p, defined as

$$C_p = \left(p_w - P_1\right) \Big/ \left(\rho U_t^2 / 2\right) \tag{4}$$

where p_w and P_1 are the ensemble-averaged wall pressure and the inlet stagnation pressure, respectively.

In the case of τ > 0.5 mm (0.4 percent of tip chord) for the axial flow rotor, as seen in Fig. 11(b), a pressure trough extends from the minimum pressure region near the blade suction side to the rotor exit. It should be noted that the pressure trough following the minimum pressure region corresponds to a locus of the tip leakage vortex core (Inoue and Kuroumaru, 1989).

On the other hand, the pressure trough in the diagonal flow rotor with the tip clearance of τ > 0.5 mm (0.3 percent of tip chord) appears clearly at the fore part of the rotor passage and decays at the aft part of the passage, as seen in Fig. 11(a). This implies that the tip leakage vortex formed near the leading edge disappears at the aft part of the rotor passage. This behavior of the tip leakage vortex corresponds well to the fact that no rolling-up of the vortex is observed in the secondary flow fields downstream of the diagonal flow rotor (Fig. 7).

Leakage Flow Fields Inside Rotor

As mentioned above, the behavior of the tip leakage flow in the diagonal flow rotor has been found to be substantially different from that in the axial flow rotor. It is very difficult to experimentally investigate what causes the behavior. In the following, comparisons of the computational results between the diagonal and axial flow rotors with the tip clearance of 2.0 mm are presented to look deep into the cause of the behavior.

Figure 12 shows contours of the static pressure coefficient on the casing wall and distributions of the absolute streamwise vorticity along a tip leakage vortex core. The static pressure coefficient is defined by Eq. (4), and its increment in the contours is the same as that for the experimental results shown in Fig. 11. The absolute streamwise vorticity is defined and normalized as

$$\xi_s = \frac{\vec{\xi} \cdot \vec{w}}{2\omega |\vec{w}|} \tag{5}$$

where $\vec{\xi}$ and $\vec{w}$ are vectors of the absolute vorticity and the relative flow velocity, respectively, and ω is the angular velocity magnitude of the rotor. In Fig. 12 the streamwise vorticity distribution is shown by colors only along the leakage vortex core, and a few leakage streamlines surrounding the vortex core are indicated by violet lines. The trajectory of the leakage vortex core is approximately defined by the streamline that has the minimum curvature and emanates from the tip clearance near the leading edge. In the computational results for both the diagonal and axial flow rotors, the pressure trough on the casing wall is captured, and its behavior corresponds well to the experimental results shown in Fig. 11.

The well-known behavior of the tip leakage flow in the axial flow rotor is obtained in the computational result shown in Fig. 12(b). The rolling-up of the tip leakage vortex, which can be observed as the coiling of the leakage streamlines around the vortex core, is clearly seen both in the rotor passage and downstream of the rotor. The leakage vortex core traces the casing pressure trough well. The streamwise vorticity decays gradually along the vortex core.

The behavior of the leakage vortex different from that in the axial flow rotor is captured in the diagonal one shown in Fig. 12(a). The rolling-up of the leakage vortex is observed at the fore part of the rotor passage where the vortex core traces the pressure trough. As the pressure trough becomes smaller, however, the leakage vortex core curves abruptly, and the streamwise vorticity along it decreases to about zero. Then, the rolling-up of the vortex seems to disappear al the aft part of the passage.

In order to investigate the rolling-up of the leakage vortex quantitatively, we introduce a normalized helicity similar to that used by Levy et al. (1990). The normalized helicity used in the present paper is defined as

$$H_n = \frac{\vec{\xi} \cdot \vec{w}}{|\vec{\xi}||\vec{w}|} \tag{6}$$

where $\vec{\xi}$ and $\vec{w}$ denote the vectors of the "absolute" vorticity and the "relative" flow velocity, respectively, in the same way as Eq. (5). Note that the normalized helicity is not defined by the "relative vorticity", but by the "absolute vorticity", considering that secondary flow fields in the rotors are dominated by the component of "absolute vorticity" along the "relative flow" direction. The normalized heticity is the cosine of the angle between the absolute vorticity and relative velocity vectors. This means that the magnitude of the normalized helicity tends to unity in the vortex core, and its sign indicates the direction of swirl of the vortex relative to the streamwise velocity component. In contrast to the streamwise vorticity defined by Eq. (5), the normalized helicity allows us to quantitatively examine the strength of the vortex rolling-up regardless of the decay of vorticity in the streamwise direction.

Figure 13 shows distributions of the normalized helicity along the tip leakage flow together with the casing wall pressure contours. In the figure, red denotes the normalized helicity of unity, and green denotes that of zero. For the axial flow rotor the normalized helicity is about unity along the leakage flow to the downstream of the rotor, which means that the leakage vortex is tightly rolled up to the downstream of the rotor. This corresponds well to the experimental result downstream of the rotor shown in Fig. 9(c).

On the other hand, in the diagonal flow rotor shown in Fig. 13(a), the nature of the leakage vortex is substantially different from that in the axial flow rotor. The strong rolling-up of the leakage vortex with the normalized helicity of about unity is formed from just downstream of the leading edge to about 35 percent of the meridional chord, thus causing the steep pressure trough on the casing wall. Near 50 percent of the meridional chord, however, a gradual decrease in the normalized helicity occurs and corresponds to the decay of the pressure trough. Then, the nature of the leakage vortex changes drastically at the aft part of the passage: the leakage vortex is expanded remarkably, and the vortex core is occupied by the flows with negative normalized helicity, thus being destroyed. This change corresponds well to the disappearance of the casing pressure trough. It seems that the significant change in the nature of the leakage vortex indicates the occurrence of "vortex breakdown".

In order to confirm the occurrence of vortex breakdown in the diagonal flow rotor, the detailed flow structure in the leakage vortex is investigated on crossflow planes. The planes are located in four positions nearly perpendicular to the leakage vortex core, as shown by planes I, II, III and IV in Figs. 14, 15 and 16. In these figures the same leakage streamlines as Fig. 13 are shown by black lines. For the diagonal flow rotor, planes III and IV are located in the region where the "vortex breakdown" seems to occur.

Figure 14 shows distributions of a total pressure loss coefficient on the crossflow planes. The total pressure loss coefficient is defined as

$$\zeta_p = \frac{\omega(r c_\theta - r_1 c_{\theta 1}) - (P - P_1)/\rho}{U_t^2/2} \tag{7}$$

where r is the radius from the axis of rotation, c_θ is the absolute tangential velocity component, P is the total pressure, and subscript of 1 denotes the rotor inlet. Only the region with the total pressure loss coefficient above 0.2 is shown in Fig. 14. For both the diagonal and axial flow rotors, it is clearly seen that the high loss fluid accumulates in the tip leakage vortex. This means that the size of the high loss region accumulating on the casing corresponds to the leakage vortex size. In contrast to the axial flow rotor in which the high loss region in the leakage vortex grows gradually in the streamwise direction, the extremely large spread of the high loss region is observed on planes III and IV in the diagonal flow rotor. It should be realized that in the diagonal flow rotor the large expansion of the leakage vortex occurs at the aft part of the rotor passage. This expansion of the vortex size corresponds well to the experimental results: the large growth of the casing wall boundary layer (Fig. 5(a)), and the large spread of the low-energy fluid (Fig. 8) downstream of the rotor.

Distributions of the absolute vorticity on the crossflow planes are shown in Fig. 15. The vorticity is normalized by twice the angular velocity of the rotor, 2ω. For the axial flow rotor, the absolute vorticity in the leakage vortex decays in the streamwise direction, but the vortex core can be observed as the region with the concentrated vorticity. On the other hand, in the diagonal flow rotor the drastic change in the leakage vortex structure is observed on crossflow planes III and IV: the high vorticity region due to the leakage flow is spread out, and the vortex core with the concentrated vorticity is not observed in the leakage flow field. It is found that the core of the leakage vortex disappears at the aft part of the passage in the diagonal flow rotor. The disappearance of the vortex core corresponds to the experimental results, namely no rolling-up of the leakage vortex downstream of the rotor (Fig. 7), and the disappearance of the casing pressure trough (Fig. 11(a)). It should be noted that the normalized helicity distribution along the leakage flow, shown in Fig. 13(a), indicates the disappearance of the leakage vortex core, also.

Figure 16 shows distributions of the relative velocity, w/U_t, normalized by the blade tip speed at the rotor exit. For the diagonal flow rotor, as compared with the axial one, the region with lower relative velocity is observed in the leakage flow on crossflow planes III and IV. At plane IV the velocity in this region is so low as to decrease almost to zero, and the region is spread out remarkably. It should be realized that the low-velocity region appears in the leakage flow away from the casing wall. In Fig. 17 the low-velocity region is shown by a blue isosurface of the relative velocity of $w/U_t = 0.1$, and the leakage streamlines with the normalized helicity distributions are also presented. Figure 17 indicates that the low-velocity region appears along the leakage vortex in the aft part of the rotor passage and causes the expansion of the vortex. It should be noted that the region contains reverse flows (not shown in Figs. 16 and 17). The low-velocity region apparently results in the large growth of the casing wall boundary layer. Figure 18 shows the streamwise distributions of the meridional displacement thickness of the casing wall boundary layer in the diagonal and axial flow rotors. In the figure the abscissa denotes the meridional distance from the leading edge. The displacement thickness is evaluated by averaging the computational results in the tangential direction. In Fig. 18 it is observed that the growth of the boundary layer in the diagonal flow rotor is much larger than that in the axial one, and its thickness distribution has a maximum in the aft part of the passage

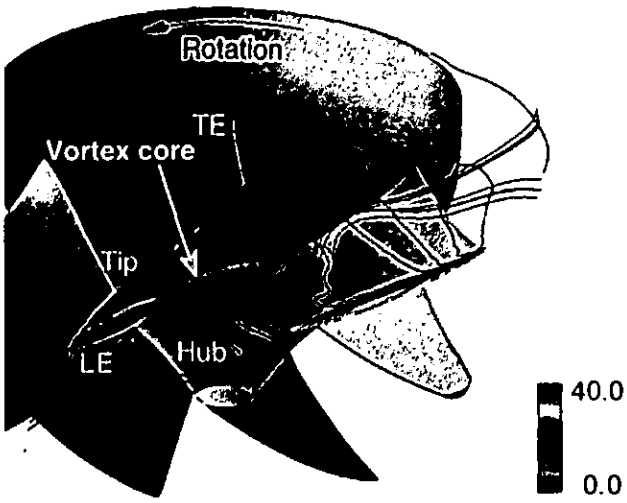

(a) Diagonal flow rotor with tip clearance of 2.0 mm

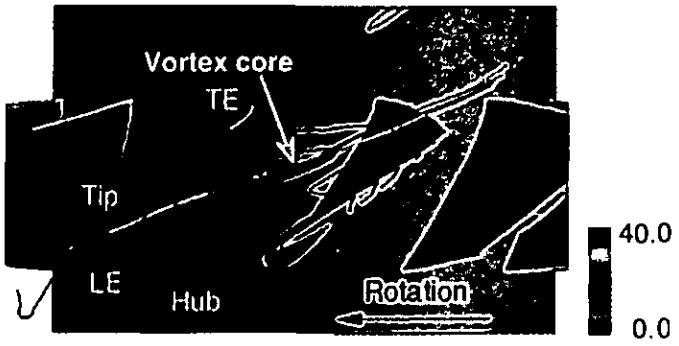

(b) Axial flow rotor with tip clearance of 2.0 mm

Fig. 12 Tip leakage vortex core with absolute streamwise vorticity distribution, leakage streamlines surrounding vortex core, and casing wall pressure distribution

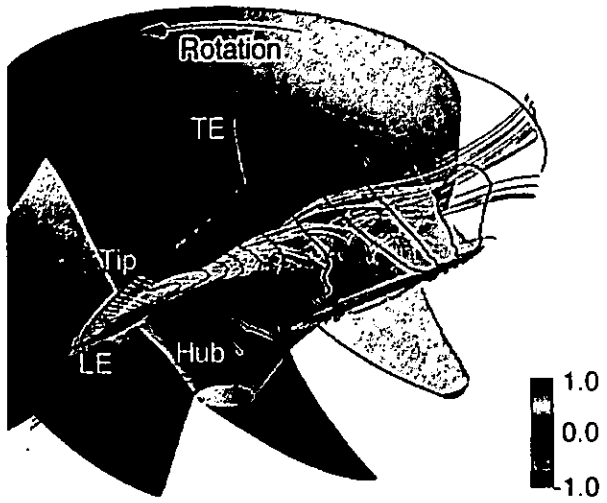

(a) Diagonal flow rotor with tip clearance of 2.0 mm

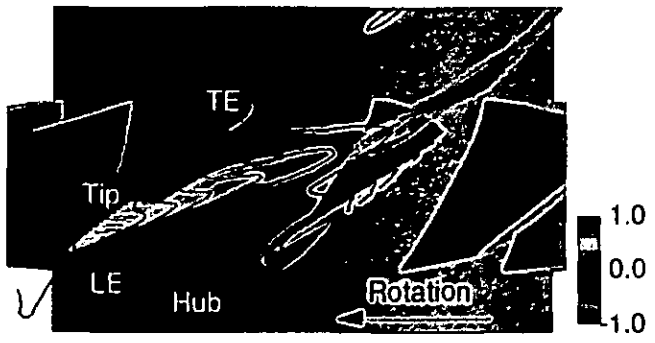

(b) Axial flow rotor with tip clearance of 2.0 mm

Fig. 13 Normalized helicity distribution along tip leakage flow and casing wall pressure distribution

where the low-velocity region appears. Moreover, it is obvious that the fluid in the low relative velocity region has a large tangential component of the absolute velocity, like the wake of the blade. This fact corresponds well to the experimental result that the absolute tangential velocity downstream of the diagonal flow rotor increases considerably in the casing wall boundary layer as seen in Fig. 5(b).

From the significant changes in the nature of the tip leakage vortex, namely the large expansion of the vortex, the disappearance of the vortex core and the appearance of the low relative velocity region in the vortex, it is hard to escape the conclusion that the "breakdown" of the tip leakage vortex occurs in the diagonal flow rotor. The appearance of the low-velocity region with reverse flow is evidence of the fact that the large expansion of the vortex and the disappearance of the vortex core do not result from the diffusion. The "breakdown" of the tip leakage vortex can be regarded as a phenomenon similar to the breakdown of the leading edge vortices on a delta type wing. The vortex breakdown on a delta type wing is a well-known phenomenon and has been investigated by many experimental and numerical works (Rom, 1992). It is evident that not only does the "vortex breakdown" result in the behavior of the tip leakage flow substantially different from that in the axial flow rotor, but also it influences the overall performance of the rotor. The large growth of the casing wall boundary layer due to the vortex breakdown causes the large reduction of efficiency with the tip clearance: for the present diagonal flow rotor, an increase in the clearance/chord ratio from 0.3 percent to 1.3 percent brings about 6 percent reduction of efficiency at the design flow rate, as seen in Fig. 2, which is about three times as large as that of the axial flow rotor. On the other hand, the disappearance of the leakage vortex core due to the breakdown gives the diagonal flow rotor a superiority to the axial one: the noise level of the diagonal flow rotor is considerably low, compared with the axial one (Inoue et al., 1984). The low level of noise appears to result from the fact that the vortex breakdown leads to the loss of the pressure gradient around the vortex core, which can be observed in the casing wall pressure distribution (Fig. 12(a)), and so pressure fluctuations induced by the leakage vortex decrease on solid walls.

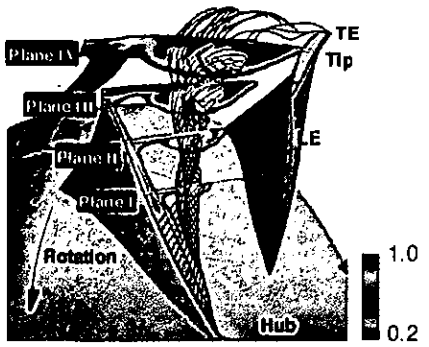

(a) Diagonal flow rotor with tip clearance of 2.0 mm

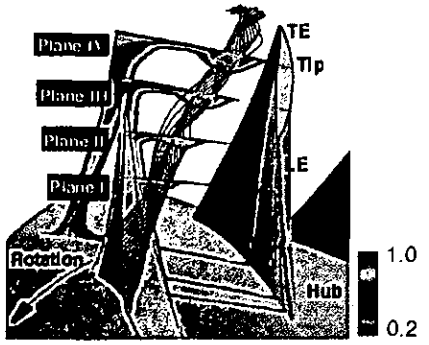

(b) Axial flow rotor with tip clearance of 2.0 mm

Fig. 14 Total pressure loss coefficient diatributions on crossflow planes perpendicular to tip leakage vortex

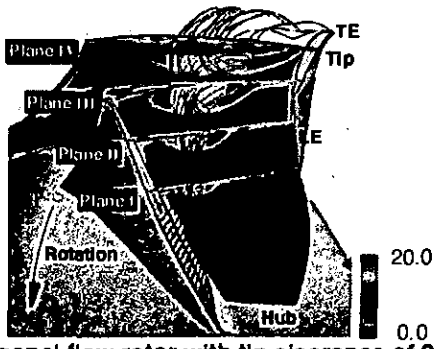

(a) Diagonal flow rotor with tip clearance of 2.0 mm

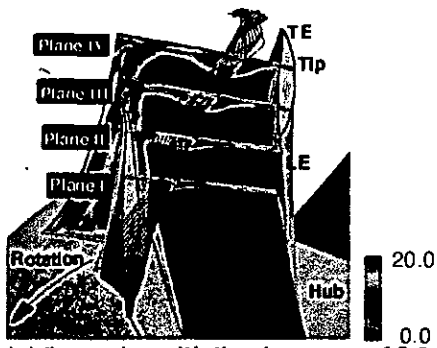

(b) Axial flow rotor with tip clearance of 2.0 mm

Fig. 15 Absolute vorticity distributions on crossflow planes perpendicular to tip leakage vortex

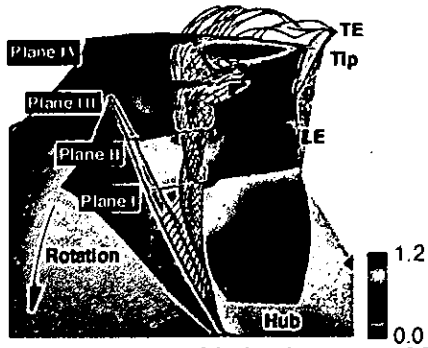

(a) Diagonal flow rotor with tip clearance of 2.0 mm

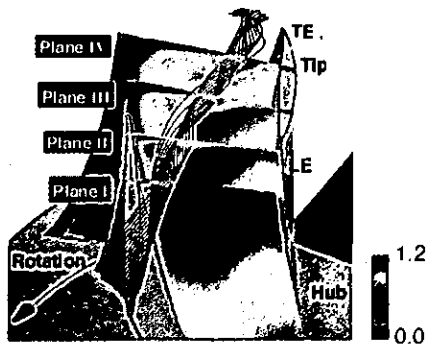

(b) Axial flow rotor with tip clearance of 2.0 mm

Fig. 16 Relative velocity distributions on crossflow pisnes perpendicular to tip leakage vortex

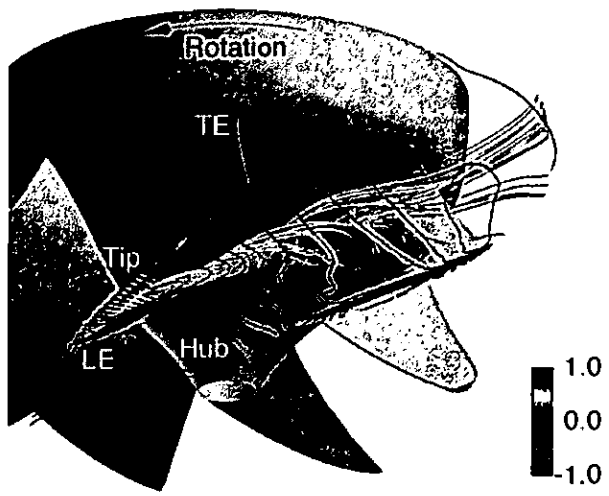

Fig. 17 Isosurface of relative velocity of w/U_t = 0.1 (shown by blue surface) and normalized helicity distributions along tip leakage flow for diagonal flow rotor with tip clearance of 2.0 mm

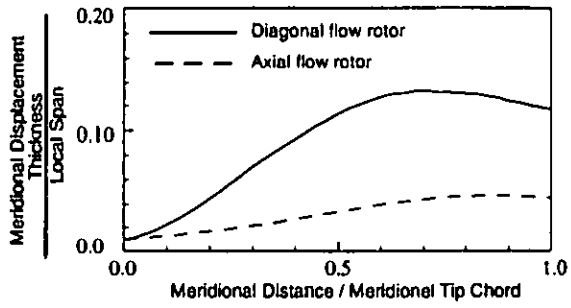

Fig. 18 Meridional displacement thickness distributions of casing wall boundary layer in diagonal and axial rotors with tip clearance of 2.0 mm

In order to simulate the tip leakage flow fields accurately, special attention must be paid to grid resolution. Not only the wall boundary layers but the main flow region away from the wall requires the high grid resolution, because the tip leakage vortex consisting of the concentrated vorticity is formed outside the boundary layer. In the present simulations the tip leakage vortices, including the vortex breakdown, are captured relatively well. However, the computational grids used for the present simulations are not sufficient to capture the more detailed flow structure, such as the detailed structure in the vortex breakdown region. In addition to the calculations presented in this paper, other calculations were performed using a coarse grid system in which the main and embedded grids consisted of 59(I)×43(J)×37(K) cells and 31(I)×11(J)×15(K) cells, respectively. The simulation with the coarse grid system captured no breakdown of the tip leakage vortex in the diagonal flow rotor. It should be noted that the high grid resolution is indispensable to the tip leakage flow simulation, including the vortex breakdown.

CONCLUSIONS

Experimental and computational results of the tip leakage flow in a diagonal flow rotor have been compared with those in an axial flow rotor. It was found out that "breakdown" of the tip leakage vortex occurs at the aft part of the passage in the diagonal flow rotor. The "vortex breakdown" causes significant changes in the nature of the tip leakage vortex: disappearance of the vortex core, large expansion of the vortex, and appearance of low relative velocity region in the vortex. These changes result in the following behavior of the tip leakage flow substantially different from that in the axial flow rotor:

(1) Because of the disappearance of the vortex core with the concentrated vorticity, the rolling-up of the tip leakage vortex is not observed downstream of the diagonal flow rotor.

(2) The disappearance of the vortex core leads to the loss of the pressure gradient induced by the concentrated vorticity, so that the pressure trough vanishes from the casing wall at the aft part of the rotor passage.

(3) The disappearance of the vortex core seems to result in the fact that the noise level of the diagonal flow rotor is considerably low, compared with the axial one.

(4) Because of the large expansion of the leakage vortex caused by the low relative velocity region with reverse flow, the low-energy fluid due to the leakage flow is spread out from the casing to about a half of span. As a result, much larger growth of the casing wall boundary layer occurs, compared with the axial flow rotor.

(5) Downstream of the diagonal flow rotor, the absolute tangential velocity increases considerably in the casing wall boundary layer, because the fluid in the low relative velocity region has a large tangential component of the absolute velocity, like the wake.

(6) The large growth of the casing wall boundary layer causes large reduction of efficiency with the tip clearance: the reducing rate of efficiency is about three times as large as that of the axial flow rotor.

In order to examine the rolling-up of the tip leakage vortex quantitatively, we have introduced the normalized helicity defined by the vectors of the absolute vorticity and the relative velocity. It should be noted that the normalized helicity is useful in investigating the nature of the tip leakage vortex.

In the present study the occurrence of "breakdown" of the tip leakage vortex in the diagonal flow rotor has been found out. However, its mechanism has been unresolved. Many attempts must be made to investigate the "vortex breakdown" in the tip leakage flows.

ACKNOWLEDGMENTS

The present research was supported by the Ministry of Education through the Grant-in-Aid for Scientific Research (C). The authors gratefully acknowledge the research fund from Harada Memorial Foundation.

REFERENCES

Adamczyk, J. J., Celestina, M. L., and Greitzer, E. M., 1993, "The Role of Tip Clearance in High-Speed Fan Stall," ASME Journal of Turbomachinery, Vol. 115, pp. 28-38.

Anderson, W. K., Thomas, J. L., and van Leer, B., 1986, "Comparison of Finite Volume Flux Vector Splittings for the Euler Equations," AIAA Journal, Vol. 24, pp. 1453-1460.

Baldwin, B. S., and Lomax, H., 1978, "Thin Layer Approximation and Algebraic Model for Separated Turbulent Flow," AIAA Paper No. 78-257.

Chakravarthy, S. R., 1986, "The Versatility and Reliability of Euler solvers Based on High-Accuracy TVD Formulations," AIAA Paper No. 86-0243.

Chen, G. T., Greitzer, E. M., Tan, C. S., and Marble, F. E., 1991, "Similarity Analysis of Compressor Tip Clearance Flow Structure," ASME Journal of Turbomachinery, Vol. 113, pp. 260-271.

Dawes, W. N., 1987, "A Numerical Analysis of the Three-Dimensional Viscous Flow in a Transonic Compressor Rotor and Comparison With Experiment," ASME Journal of Turbomachinery, Vol. 109, pp. 83-90.

Foley, A. C., and Ivey P. C., 1996, "Measurement of Tip-Clearance Flow in a Multistage, Axial Flow Compressor," ASME Journal of Turbomachinery, Vol. 118, pp. 211-217.

Furukawa, M., Yamasaki, M., and Inoue, M., 1991, "A Zonal Approach for Navier-Stokes Computations of Compressible Cascade Flow Fields Using a TVD Finite Volume Method," ASME Journal of Turbomachinery, Vol. 113, pp. 573-582.

Furukawa, M., Nakano, T., and Inoue, M., 1992, "Unsteady Navier-Stokes Simulation of Transonic Cascade Flow Using an Unfactored Implicit Upwind Relaxation Scheme With Inner Iterations," ASME Journal of Turbomachinery, Vol. 114, pp. 599-606.

Furukawa, M. Inoue, M., Kuroumaru, M., and Saiki, K., 1995a, "Behavior of Tip Leakage Flow in a Diagonal Flow Impeller with

High Specific Speed," Proceedings of the 1995 Yokohama International Gas Turbine Congress, Vol. 1, pp. 109-114.

Furukawa, M., Saiki, K., and Inoue, M., 1995b, "Numerical Simulation of Three-Dimensional Viscous Flow in Diagonal Flow Impeller," in : *Numerical Simulations in Turbomachinery*, ASME FED-Vol. 227, pp. 29-36.

Goto, A., 1992a, "Study of Internal Flows in a Mixed-Flow Pump Impeller at Various Tip Clearances Using Three-Dimensional Viscous Flow Computations," ASME Journal of Turbomachinery, Vol. 114, pp. 373-382.

Goto, A., 1992b, "The Effect of Tip Leakage Flow on Part-Load Performance of a Mixed-Flow Pump Impeller," ASME Journal of Turbomachinery, Vol. 114, pp. 383-391.

Hah, C., 1986, "A Numerical Modeling of Endwall and Tip-Clearance Flow of an Isolated Compressor Rotor," ASME Journal of Engineering for Gas Turbines and Power, Vol. 108, pp. 15-21.

Inoue, M., Ikui, T., Kamada, Y., and Tashiro, M., 1980, "A Quasi Three-Dimensional Design of Diagonal Flow Impellers by Use of Cascade Data," Proceedings of the 10th Symposium, The International Association for Hydraulic Research Vol. 1, pp. 403-414.

Inoue, M., Wu, K-C., Kuroumaru, M., Furukawa, M., Fukuhara, M., and Ikui, T., 1984, "A Design of Diagonal Impeller by Means of SCM and Cascade Data," Proceedings of China-Japan Joint Conference on Hydraulic Machinery and Equipment, Vol. 1, pp. 21-30.

Inoue, M., Kuroumaru, M., and Fukuhara, M., 1986, "Behavior of Tip Leakage Flow Behind an Axial Compressor Rotor," ASME Journal of Engineering for Gas Turbines and Power, Vol. 108, pp. 7-14.

Inoue, M., and Kuroumaru, M., 1989, "Structure of Tip Clearance Flow in an Isolated Axial Compressor Rotor," ASME Journal of Turbomachinery, Vol. 111, pp. 250-256.

Inoue, M., and Furukawa, M., 1994, "Artificial Dissipative and Upwind Schemes for Turbomachinery Blade Flow Calculations," VKI, Lecture Series, No. 1994-06.

Kang, S., and Hirsch, C., 1996, "Numerical Simulation of Three-Dimensional Viscous Flow in a Linear Compressor Cascade With Tip Clearance," ASME Journal of Turbomachinery, Vol. 118, pp. 492-505.

Klapproth, J. F., 1959, Discussion in : Lieblein, S., "Loss and Stall Analysis of Compressor Cascades," ASME Journal of Basic Engineering, Vol. 81, pp. 387-400.

Kuroumaru, M., Inoue, M., Higaki, T., Abd-Elkhalek, F. A., and Ikui, T., 1982, "Measurements of Three-Dimensional Flow Field Behind an Impeller by Means of Periodic Multi-Sampling of a Slanted Hot Wire," Bulletin of the JSME, Vol. 25, No. 209, pp. 1674-1681.

Lakshminarayana, B., Zaccaria, M., and Marathe, B., 1995, "The Structure of Tip Clearance Flow in Axial Flow Compressors," ASME Journal of Turbomachinery, Vol. 117, pp. 336-347.

Levy, Y., Degani, D., and Seginer, A., 1990, "Graphical Visualization of Vortical Flows by Means of Helicity," AIAA Journal, Vol. 28, pp. 1347-1352.

Moyle, I. N., Walker, G. J., and Shreeve, R. P., 1992, "Stator Averaged Rotor Blade to Blade Near Wall Flow in a Multistage Axial Compressor With Tip Clearance Variation," ASME Journal of Turbomachinery, Vol. 114, pp. 668-674.

Murthy, K. N. S., and Lakshminarayana, B., 1986, " Laser Doppler Velocimeter Measurement in the Tip Region of a Compressor Rotor," AIAA Journal, Vol. 24, pp. 807-814.

Osher, S., and Chakravarthy, S. R., 1983, "Upwind schemes and Boundary Conditions with Applications to Euler Equations in General Coordinates," Journal of Computational Physics, Vol.50, pp. 447-481.

Rains, D. A., 1954, "Tip Clearance Flows in Axial Flow Compressors and Pumps," California Institute of Technology, Hydrodynamics and Mechanical Engineering Laboratories, Report No. 5.

Roe, P. L., 1981, "Approximate Riemann Solvers, Parameter Vectors, and Difference Schemes," Journal of Computational Physics, Vol. 43, pp. 357-372.

Rom, J., 1992, *High Angle of Attack Aerodynamics : Subsonic, Transonic, and Supersonic Flows*, Springer-Verlag, New York.

Smith, L. H., Jr., 1970, "Casing Boundary Layers in Multistage Axial-Flow Compressors," in : *Flow Research on Blading*, Ed. Dzung, L. S., Elsevier, New York, pp. 275-304.

Stauter, R. C., 1993, "Measurement of the Three-Dimensional Tip Region Flow Field in an Axial Compressor," ASME Journal of Turbomachinery, Vol. 115, pp. 468-476.

Storer, J. A., and Cumpsty, N. A., 1991, "Tip Leakage Flow in Axial Compressors," ASME Journal of Turbomachinery, Vol. 113, pp. 252-259.

Suder, K. L., and Celestina, M. L., 1996, "Experimental and Computational Investigation of the Tip Clearance Flow in a Transonic Axial Compressor Rotor," ASME Journal of Turbomachinery, Vol. 118, pp. 218-229.

Swanson, R. C., and Turkel, E., 1993, "Aspects of a High-Resolution Scheme for the Navier-Stokes Equations," AIAA Paper No. 93-3372-CP.

Van Leer, B., Thomas, J. L., Roe, P. L., and Newsome, R. W., 1987, "A Comparison of Numerical Flux Formulas for the Euler and Navier-Stokes Equations," AIAA Paper No. 87-1104.

Zierke, W.C., Farrell, K.J., and Straka, W.A., 1995, "Measurement of the Tip Clearance Flow for a High-Reynolds-Number Axial Flow Rotor," ASME Journal of Turbomachinery, Vol. 117, pp. 522-532.